

CONFERENCES AND SYMPOSIA

PACS numbers: 71.35.Ji, 71.35.Lk, 73.21.Fg, 73.43.Lp

Exciton condensates in integer and fractional quantum Hall dielectrics *

A.V. Larionov, A.V. Gorbunov, L.V. Kulik

DOI: https://doi.org/10.3367/UFNe.2025.04.040008

Contents

Abstract. A review of experimental studies of the properties of a recently discovered new coherent collective state, a magnetoexciton condensate, is presented. Condensation occurs at temperatures below 1 K in a Fermi system, an integer quantum Hall dielectric (filling factor $\nu = 2$), as a result of the formation of a dense ensemble of long-lived triplet spin cyclotron magnetoexcitons, composite bosons. Using a high-aperture, high-resolution optical system, the formation and spreading of dense photoexcitation ensembles in real space in integer and fractional quantum Hall dielectrics with filling factors $\nu = 2$ and $\nu = 1/3$ is visualized. The correlation between the transport and coherence properties of these ensembles is analyzed.

Keywords: magnetoexcitons, quantum Hall insulator, collective excitations, magnetoexciton condensate

1. Introduction

The fundamental question of the possibility of Bose–Einstein condensation (BEC) of excitons in solids attracted the attention of theorists in the early 1960s [1–3], and after the publication of the pioneering works of L.V. Keldysh and coauthors [4, 5], it became one of the most actively discussed topics in the scientific literature. In order for condensation to occur, it is necessary to create a dense long-lived ensemble of excitons and cool it to the temperature of the phase transition into the condensed state, as was later achieved for atomic systems in magnetic traps [6, 7]. Experimental searches for excitonic BEC in high-quality single crystals (CdSe, CuCl, and especially Cu_2O), initiated in the 1970s, continue to this day, but for various reasons have not yet yielded positive results. A review of studies in this field over a 30-year period and a discussion of prospects for the near future can be found in Ref. [8]. Significant progress toward the creation of dense excitonic ensembles was achieved in ultra-high-purity indirect-gap semiconductors such as Ge and Si. However, because of valley degeneracy in the conduction band of Ge and Si, the experimentally observed phase transition is not into a Bose–Einstein condensate, but into a new condensed state of excitonic matter, namely, the electron-hole liquid [9]. All attempts to resolve the problem of valley degeneracy by means of uniaxial compression or an external magnetic field led only to partial lifting of the degeneracy and to the observation of non-Boltzmann exciton statistics [10]. Thus, the creation of a Bose–Einstein condensate of excitons in three-dimensional solid-state systems has not yet been successful.

In the mid-1970s, theoretical studies appeared in which attention was drawn to the promise of two-dimensional (2D) spatially separated electron-hole layers for the observation of BEC and superfluidity effects [11, 12]. With the development of semiconductor nanostructure technology in the 1990s, active experimental investigations aimed at the search for excitonic BEC in 2D systems began. In this context, spatially indirect (dipolar) excitons, in which the electron and hole are spatially separated under the action of an external electric field, became a popular object of study. Owing to the reduced overlap of the electron and hole wave functions, the lifetime of an indirect exciton can reach tens of microseconds instead of the conventional $\leqslant 100$ ps. Such excitons are substantially

A.V. Larionov [(a)], **A.V. Gorbunov** [(b)], **L.V. Kulik** [(c)]
Osipyan Institute of Solid State Physics, Russian Academy of Sciences, ul. Akademika Osipyana 2, 142432 Chernogolovka, Moscow region, Russian Federation
E-mail: [(a)] larionov@issp.ac.ru, [(b)] gorbunov@issp.ac.ru, [(c)] kulik@issp.ac.ru

Received 11 July 2025
Uspekhi Fizicheskikh Nauk **196** (5) 490 – 505 (2026)
Translated by the authors

* This review is based on the report presented for the Scientific Session of the Physical Sciences Division of the Russian Academy of Sciences (PSD RAS), on April 23, 2025 (see *Physics–Uspekhi* **69** (5) 419 (2026); *Uspekhi Fizicheskikh Nauk* **196** (5) 449 (2025)).

easier to cool, bringing their temperature closer to the temperature of the crystal lattice. However, despite the considerable activity in this field, there is still no consensus in the scientific community regarding the successful condensation of dipolar excitons. Undoubted successes in the physics of two-dimensional excitons have been achieved in the creation and investigation of exciton-polariton nonequilibrium condensates in quantum wells placed inside Bragg resonators [13]. Owing to the substantial mixing of excitons with light, exciton-polariton condensates are close in their properties to laser systems; therefore, the question of the possibility of condensation of 2D excitons themselves remains open at present.

This review presents new results related to experiments on the condensation of 2D magnetoexcitons, which are excitations in two-dimensional electron systems (2DESs) placed in an external quantizing magnetic field. It should be noted that magneto-optical investigations of 2DESs have been ongoing for a long time, and the corresponding bibliography is rather extensive (see, for example, the reviews [14, 15]). Theoretically, the problem of a 2D Wannier–Mott exciton in a transverse magnetic field was considered in Ref. [16]. At that time, the prospects for magnetoexciton condensation appeared highly promising: the properties of a 2D gas of such excitations were found to be close to those of an ideal Bose gas [17]. However, in experiments, the action of a magnetic field on an exciton formed by a hole in the valence band and an electron in the conduction band, even in the case of long-lived dipolar excitons in GaAs/AlGaAs double quantum wells, did not lead to condensation [18].

Relatively recently, the idea of condensation of cyclotron magnetoexcitons was proposed, in which the electron and hole are located on different Landau levels in the conduction band [19]. Specifically, this concerns a quantum Hall 2DES in which magnetoexcitons are excitations in the conduction band formed by an electronic vacancy on a 'lower' Landau level, i.e., below the Fermi level (hereafter, for brevity, a Fermi hole), and an electron in another (orbital or spin) state with higher energy. A quantum Hall insulator is formed when the Landau level(s) are completely filled with electrons: filling factors $\nu = 2, 4\ldots$ In a quantum Hall insulator with $\nu = 2$, the electronic excitations are magnetoexcitons formed by an excited electron on the empty first Landau level and a Fermi hole on the completely filled zeroth Landau level (Fig. 1a). The excitation spectrum of the quantum Hall insulator contains two types of cyclotron magnetoexcitons: a spin-singlet magnetoexciton with total spin $S = 0$ and a spin-triplet magnetoexciton with total spin $S = 1$. The spin-singlet magnetoexciton is nothing other than a magnetoplasmon, i.e., a spinless excitation whose energy at zero wave vector, according to Kohn's theorem, is equal to the single-particle cyclotron energy [20, 21]. The components of the triplet spin exciton, for which the spin projection onto the magnetic-field direction is $S_z = -1, 0, +1$, are energetically separated from one another by the Zeeman gap. At zero generalized wave vector, $(q = 0)$, and even at other relevant values, $q \leqslant 1/l_{\mathrm{B}}$ ($l_{\mathrm{B}} = \sqrt{\hbar c/eB}$ is the magnetic length), the entire triplet in $\mathrm{GaAs/Al}_x\mathrm{Ga}_{1-x}\mathrm{As}$ heterostructures lies below the empty Landau level, i.e., has an energy lower than the cyclotron gap by an additional 'binding energy' determined by Coulomb correlations in the 2DES [22–24]. This negative 'Coulomb shift' makes it possible to regard the spin cyclotron exciton (SCE) component with $S_z = +1$ as the

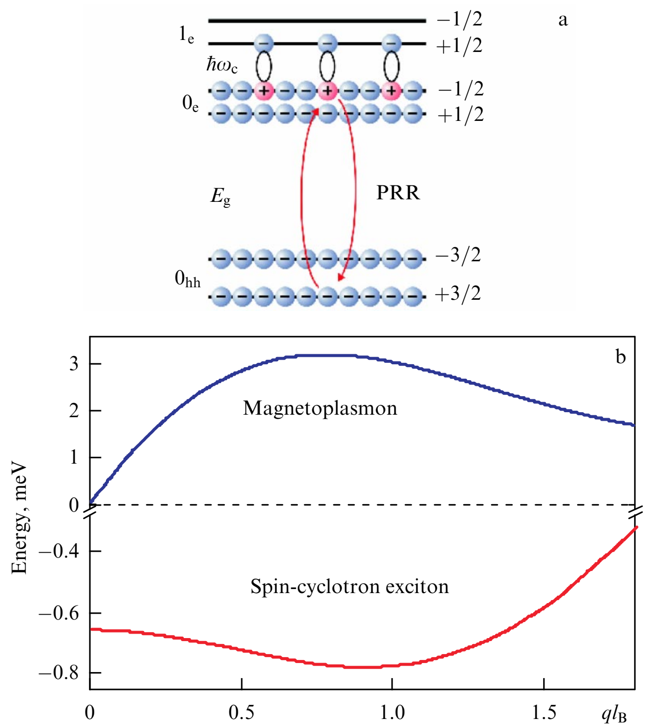

Figure 1. (a) Schematic of single-electron states of a quantum Hall insulator at a filling factor $\nu = 2$ under conditions of excitation of a triplet spin cyclotron magnetoexciton (SCE). On the left, the numbers of Landau levels for an electron in the conduction band (0_e, 1_e) and a heavy hole in the valence band (0_{hh}) are indicated; on the right, the values of the spin projection S_z are shown. Curved arrows illustrate the virtual absorption and re-emission of a photon during PRR registration. E_g is the band gap, $\hbar\omega_c$ is the cyclotron energy. (b) Results of calculating the dispersion dependence of two-particle excitations in a 32-nm-wide QW in a magnetic field of 4.2 T [26].

lowest-energy[1] excitation at $\nu = 2$. Unlike the magnetoplasmon, the SCE is not optically active. It is a so-called 'dark' exciton, since its radiative recombination is forbidden in the dipole approximation. Nevertheless, by means of dipole-allowed interband optical transitions between discrete states of heavy holes in the valence band (corresponding to Landau levels with numbers $n_{\mathrm{L}} > 1$) and states of conduction-band electrons, it is possible to create a nonequilibrium ensemble of such magnetoexcitons [25]. The main channel for changing the spin of the 2DES is provided by spin-flip processes of the photoexcited hole due to the strong spin-orbit interaction in the valence band of GaAs. During the subsequent transformation of the photoexcited heavy hole from the valence band into a Fermi hole of the electronic system, which occurs owing to the recombination of electrons from the filled zeroth Landau level with the photoexcited valence-band hole, the electronic system changes its resultant spin. Since the direct relaxation of SCEs (which are also referred to as spin-flip excitons [23]) into the ground state, accompanied by the simultaneous change of orbital and spin quantum numbers, is forbidden, the lifetime of these excitations becomes extraordinarily long [19]. Another factor hindering SCE relaxation is associated with the fact that the minimum of their dispersion relation is located not at zero generalized momentum, but at $q \sim 1/l_{\mathrm{B}}$ [22] (Fig. 1b); therefore, in

[1] This is the component with a positive value of the spin projection S_z onto the magnetic-field direction, since the electron g-factor in GaAs is negative.

addition to energy, relaxation requires the transfer of a large momentum, $\sim 10^6$ cm^{-1}. As a result, the recombination times of SCEs exceed the recombination times of a photoexcited hole by approximately 10^7 times [27]. Owing to such long lifetimes, high densities of nonequilibrium SCEs, $N_{\rm ex} \sim 10^{10}$ cm^{-2}, can be created by means of low-power photoexcitation that does not overheat the 2DES.

Although spin cyclotron excitons are purely electronic excitations, they are composite bosons, since they possess integer spin and obey Bose statistics: a macroscopically large number of excitons can occupy the same quantum state. In an ensemble of SCEs, one could expect the formation of nonequilibrium bosonic condensates analogous to those formally studied as early as in Ref. [17]. However, it is known that in 2D (as well as 1D) spatially unbounded systems, thermal fluctuations destroy long-range order at any arbitrarily low but finite temperature T [28, 29]. For this reason, a Bose condensate in such systems can exist only at $T = 0$, which is of purely theoretical interest. In the 2D case, however, thermal fluctuations do not completely destroy long-range order: spatial electron–electron correlations are preserved, although they decay with distance not exponentially, as in the gaseous phase, but according to a power law. This is sufficient for a transition into a new phase that can exhibit superfluidity at finite temperature. The effect of superfluidity in 2D systems without the formation of a Bose condensate was predicted by Vadim Berezinskii [30] and independently, although somewhat later, by J. Michael Kosterlitz and David Thouless [31] (the Berezinskii–Kosterlitz–Thouless transition, BKT). According to the theory, the transition into the superfluid state is caused by the formation of topological defects, namely, vortex–antivortex pairs. To date, there already exists a substantial amount of experimental evidence for the existence of the BKT transition in various quasi-two-dimensional systems: in liquid-helium films [32], arrays of Josephson junctions [33], ultracold atomic gases [34, 35], and gases of interacting exciton polaritons [36].

The present review discusses condensation in a system of 2D fermions (2D electrons in the conduction band), brought out of equilibrium through the formation of an ensemble of long-lived spin cyclotron excitons — composite excitations obeying Bose statistics. An ensemble of spin cyclotron excitons with sufficiently high density in a quantum Hall insulator ($\nu = 2$) at temperatures below 1 K represents another example of a dense bosonic system in a degenerate two-dimensional Fermi gas, exhibiting collective bosonic properties, alongside electron–electron bilayers [37]. Recently, the experimental conditions required for the creation of a dense ensemble of magnetic excitations with spin $S = 1$ and an ultralong lifetime (spin magnetogravitons) have been determined in another type of quantum Hall insulator — the Laughlin liquid at the electronic filling factor $\nu = 1/3$ [38–41]. To date, this is the only state of anyonic matter that has been experimentally confirmed [42, 43]. In the present work, a comparative analysis of transport and coherence properties of magnetic excitations in quantum Hall insulators at filling factors $\nu = 2$ and $\nu = 1/3$ is performed.

2. Experimental methods

2.1 The choice of heterostructure

The main objects of investigation were heterostructures containing a single, symmetrically doped GaAs/AlGaAs quantum well (QW) with a width of 31 nm, with an electron concentration in the 2D channel $n_{\rm e} \cong 2 \times 10^{11}$ cm^{-2} and a dark mobility $\mu_{\rm e} = (10-20) \times 10^6$ cm^2 V^{-1} s^{-1}. Symmetric doping is necessary in order to minimize the penetration of the conduction-electron wave function into the barrier and to reduce the contribution of the random potential at the QW heterointerfaces and impurity states in the barrier to the relaxation of excited electrons. The choice of the QW width is justified by two considerations. Narrower QWs (<20 nm) do not provide the required high electron mobility, whereas wider QWs (>35 nm) do not allow one to achieve the desired degree of nonequilibrium. The reason is that the relaxation time of nonequilibrium spin-flip excitons decreases rapidly with increasing QW width due to a reduction in the depth of the Coulomb minimum in the dispersion relation [22] (Fig. 1b). It has been established experimentally that a QW width of 30–35 nm is optimal for the creation of a nonequilibrium SCE ensemble at $\nu = 2$. The relaxation time of SCEs at other integer filling factors is much shorter (see, e.g., [44]). At present, the creation of quasi-stationary nonequilibrium systems of spin cyclotron excitons with concentrations $N_{\rm ex} \geqslant 10^{10}$ cm^{-2} at integer filling factors different from $\nu = 2$ appears impossible.

For the study of magnetic excitations in the Laughlin liquid at the electronic filling factor $\nu = 1/3$, a GaAs/AlGaAs quantum well with a width of 18 nm was used, with an electron concentration in the 2D channel $n_{\rm e} \approx 0.8 \times 10^{11}$ cm^{-2} and a dark mobility $\mu_{\rm e} \approx 3.5 \times 10^6$ cm^2 V^{-1} s^{-1}.

2.2 Diagnostics of 'dark' triplet excitons

As already mentioned, spin cyclotron excitons are 'dark,' i.e., they do not interact with light in the dipole approximation. The spin-flip exciton in the quantum Hall insulator, $\nu = 2$, was first detected by means of inelastic light scattering (ILS) [45, 23]. One could attempt to diagnose it from the absorption spectrum by preparing a structure with a Bragg mirror located behind the quantum well, as was done in Ref. [46]; however, this method is technically difficult.

2.2.1 Photoinduced resonant reflection. In this context, an experimental technique of photoinduced resonant reflection (PRR) [25] was developed, by means of which it is possible to optically excite an ensemble of translationally invariant, i.e., free, SCEs, control their density, and study the kinetics of relaxation into the ground state. The proposed method is based on measurements of resonant reflection arising from direct interband dipole-allowed transitions between discrete states (Landau levels) of heavy holes in the valence band and discrete electron states (Landau levels) in the conduction band (Fig. 1a). A priori, one may expect that in a quantum Hall insulator at filling factor $\nu = 2$, the resonant reflection signal corresponding to the transition from the zeroth Landau level of heavy holes in the valence band $n_{\rm L}^{\rm hh} = 0$ to the zeroth Landau level of conduction-band electrons $n_{\rm L}^{\rm e} = 0$ should be absent, since all electronic states of the lowest electron cyclotron level are occupied. At sufficiently low temperature, the application of optical pumping, exciting electrons via dipole-allowed interband transitions to higher Landau levels $n_{\rm L}^{\rm e} > 1$, should lead to the formation of SCEs with spin projection $S_z = +1$. This exciton is the lowest-energy excited state in GaAs/AlGaAs 2DES in a magnetic field. The process of SCE formation should lead to a simultaneous reduction in the number of unoccupied states of the first electron Landau level $n_{\rm L}^{\rm e} = 1$ and to the appearance of Fermi holes at the zeroth electron Landau level $n_{\rm L}^{\rm e}=0$. Two resonant peaks should appear in the reflection spectra: a positive peak corresponding to the optical transition (0–0) from the zeroth cyclotron level of heavy holes $n_{\rm L}^{\rm hh}=0$ to the upper spin sublevel of the zeroth cyclotron level of two-dimensional electrons $n_{\rm L}^{\rm e}=0$, and a negative peak corresponding to the transition (1–1) from the first cyclotron level of heavy holes in the valence band $n_{\rm L}^{\rm hh}=1$ to the first electron cyclotron level $n_{\rm L}^{\rm e}=1$. The positive peak is responsible for the appearance and pump-induced increase in the number of Fermi holes in the upper spin sublevel of the zeroth electron cyclotron level $n_{\rm L}^{\rm e}=0$, whereas the negative peak corresponds to a decrease with increasing pumping in the number of unoccupied states at the first electron cyclotron level $n_{\rm L}^{\rm e}=1$. Thus, the photoinduced resonant reflection (PRR) method provides an indirect means of probing optically inactive SCEs using optically allowed transitions (0–0) and (1–1) from the valence band to the conduction band.

Since in experiment it is more convenient to measure a weak signal on a small background than a small difference between two large signals, in most cases the hole component of the SCE was monitored. On the other hand, measurement of the intensity of the negative PRR peak for photoexcited electrons allows a correct estimate of the achieved SCE concentration. In this case, the maximum PRR signal observed at equilibrium (with the pump switched off) serves as a reference for comparison with the maximum possible number of states in the first Landau level.

2.2.2 Photoluminescence of three-particle excitonic complexes. Another method for detecting 'dark' spin-flip excitons is related to the fact that, upon the creation of nonequilibrium excitations in the quantum Hall insulator, additional lines appear in the photoluminescence (PL) spectra associated with translationally invariant three-particle complexes formed from SCEs and a Fermi hole on the zeroth electronic Landau level [47, 48]. These lines not only serve as a kind of 'signal markers' of the appearance of spin-flip excitons in the system, but also contain valuable additional information. The point is that PRR successfully detects photoexcited Fermi holes forming part of SCEs but does not allow one to determine which generalized momentum q magnetoexcitons, containing these Fermi holes, possess. During experimental studies, it was found that, in addition to PRR, it is necessary to simultaneously record the PL spectra of the 2DES. It is from them that it becomes possible to determine the distribution function of magnetoexcitons over generalized momenta. Upon the appearance of nonequilibrium excitations in the system, features appear in the PL spectra associated with translationally invariant three-particle complexes constructed from a dark SCE and an additional Fermi hole [47, 48] (Fig. 2). There are two types of such complexes. If the spin projections of both holes onto the magnetic-field axis coincide, the two Fermi holes form a spin triplet. If, however, the spin projections are opposite, a spin singlet is formed. The hole-triplet three-particle state is a trion ('T'). The electron constituting the trion cannot participate in the plasma oscillations of the electron system. The energy of the trion does not carry information about the generalized momentum of the magnetoexciton entering it, and the intensity of the 'T' line reflects the total density of SCEs. The hole-singlet state is a plasmaron ('Pln'): the photoexcited electron from the spin cyclotron magnetoexciton can recombine with a Fermi hole

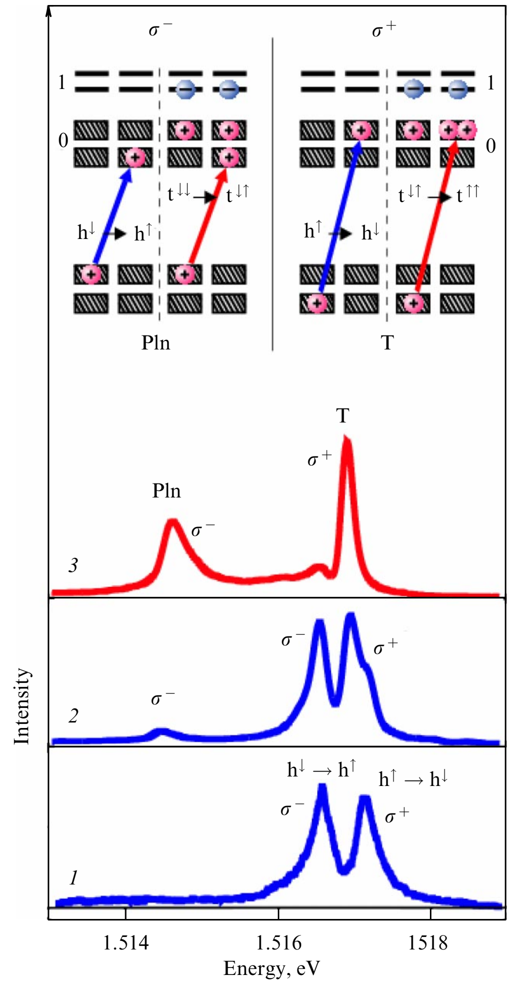

Figure 2. PL spectra: (*1*) — pulsed photoexcitation, $t_{\rm p}=10$ μs, $P_{\rm p}=100$ μW; (*2*) and (*3*) — continuous-wave photoexcitation with two spatially separated pump spots; (*2*) — $P_{\rm probe}=3$ μW, $P_{\rm pump}=0$; (*3*) — $P_{\rm probe}=3$ μW, $P_{\rm pump}=150$ μW. Top: schematic of optical transitions for two directions of circular polarization.

on the lower spin sublevel, transferring energy and momentum to a new electron–hole pair. The electron thus participates in the plasma oscillations of the entire electron system forming the Fermi hole. Approximately, the plasmaron can be considered as a magnetoplasmon bound to an additional Fermi hole. In contrast to the trion, the PL spectrum of the plasmaron carries information both about the total number of magnetoexcitons and about the energy distribution function of plasmarons. From this, in turn, the distribution function of the SCEs entering the plasmaron over generalized momenta q, which they had at the moment of plasmaron formation, is obtained [48].

2.3 Experimental geometry

2.3.1 Fiber-optic measurements. The sample with characteristic dimensions of 3×3 mm^2 was placed in an insert with liquid ^{3}He equipped with a vapor pumping system. The insert, in turn, was installed in a cryostat with liquid ^{4}He and a superconducting solenoid. The cryogenic system allowed experimental investigations to be performed down to temperatures $T\approx0.45$ K in magnetic fields B up to 14 T. Optical measurements were carried out using two multimode quartz optical fibers with a diameter of ⌀400 μm and a numerical aperture of 0.39. One fiber was used to deliver laser radiation to the sample, while the second was used to collect the emission from the sample and subsequently transfer it to the entrance slit of a diffraction spectrometer equipped with a cooled CCD detection camera. The fibers were positioned symmetrically at an angle of $\sim 10^\circ$ to the sample normal, such that the direction of the probe laser beam reflected from the sample coincided with the axis of the receiving fiber. To suppress the contribution of light scattered and reflected from the surfaces of the sample and fibers, crossed linear polarizers were used, installed between the fiber ends and the sample. Two tunable continuous-wave lasers with linewidths of 5 and 1 MHz were used: one for excitation of the 2DES (optical pumping), and the other for probing-measurement of PRR spectra and inelastic light scattering (ILS). In a number of experiments, a single-mode laser diode (wavelength $\lambda \approx 780$ nm) was used for pumping, providing nonresonant sub-barrier photoexcitation (photon energy lower than the bandgap in the AlGaAs barrier). The pump/probe spot size on the sample was $d_{\mathrm{pump}} \approx 1.5$ mm. To avoid heating effects, the pump laser power P_{pump}, exciting electrons to higher-lying Landau levels with quantum numbers $n_{\mathrm{L}}^{\mathrm{e}} > 1$, did not exceed 0.3 mW. The power of the probe laser radiation coupled into the same fiber, P_{probe}, was an order of magnitude lower. The resonant reflection spectrum was obtained by scanning the wavelength of the probe laser; the differential PRR spectrum was obtained as the difference between the resonant reflection spectra with the pump laser on and off.

For measurements in the ultralow temperature range T from 40 to 650 mK, a dilution cryostat with a superconducting solenoid was used. In this case, a pair of multimode quartz fibers with a diameter of ø200 μm and a numerical aperture of 0.22 was used for spectral measurements. The pump and probe spot size on the sample was $\cong 0.8$ mm. The pump power on the sample was $P_{\mathrm{pump}} < 10$ μW (power density $I_{\mathrm{pump}} < 2$ mW cm^{-2}), while the probe laser power was two orders of magnitude lower.

2.3.2 Spatially resolved measurements. For spatially resolved measurements, a ^{3}He insert with an optical window was fabricated, which in turn was installed in a ^{4}He cryostat with a superconducting solenoid. The experiments were performed at temperatures from 0.55 K to 1.5 K in a magnetic field up to 6 T, oriented perpendicular to the quantum well plane. A single-mode laser diode ($\lambda \approx 780$ nm) was used to form an ensemble of nonequilibrium SCEs and to excite the PL signal, while a tunable continuous-wave laser with a linewidth of 1 MHz was used to probe the resonant reflection. Inside the ^{3}He insert, a high-aperture two-lens projection system was installed, by means of which the laser radiation was focused onto the surface of the investigated sample. For precise focusing, the sample was smoothly translated along the optical axis using a mechanical translation stage. The minimum pump spot size on the sample was ≈ 5 μm. Using the same pair of lenses, the resonant reflection and PL radiation were extracted outward in the form of a parallel beam. A magnified image of the sample ($\times 23$) was projected by a long-focal-length objective onto the entrance slit of a grating spectrometer equipped with a cooled CCD camera. The image of the sample in PL light was observed either in the zero-diffraction order of the spectrometer or using a separate cooled CCD camera. The spatial resolution could reach ≈ 1 μm. Spectral selection was performed using a band-pass interference optical filter (bandwidth 10 nm). To suppress the reflected signal from the sample surface, a pair of crossed linear polarizers was used, placed outside the cryostat: one at the input in the probe laser beam, and the other at the output in the reflected beam.

2.4 Measurements of photoinduced-resonant-reflection kinetics

In measurements of PRR kinetics, the radiation of a continuous-wave pump laser was initially modulated by a mechanical chopper — a rotating disk with a radial slit: the pulse repetition period was $T_{\mathrm{p}} \approx 11$ ms, and the pulse duration was $t_{\mathrm{p}} \lesssim 3$ ms. Due to focusing of the laser spot onto the surface of the disk, the rise/fall time of the laser pulse was shortened to ≈ 2 μs. In subsequent experiments, a single-mode laser diode ($\lambda \approx 780$ nm) was used for photoexcitation, with its current modulated by a rectangular pulse generator with a rise/fall time of ≈ 10 ns. The wavelength of the probe laser was set to the maximum/minimum of the PRR spectrum to record the decay/growth curve of the signal after the end of the pump pulse, respectively. The probe laser radiation reflected from the sample surface was passed through a narrow-band interference optical filter (bandwidth ~ 1.1 nm) to suppress the pump laser light and was then focused onto the input of a silicon avalanche photodiode operating in the photon-counting regime. Using a time-gated photon counter, the PRR signal was measured and accumulated as a function of the time delay from the moment of switching off the pump laser pulse. As a result, the decay (or growth) curve of the PRR was recorded.

2.5 Measurements of spatial coherence

The interference superposition of two waves with intensities $I_1(\mathbf{r})$ and $I_2(\mathbf{r})$ in the general case leads to a distribution of the form (see, e.g., [49]):

$$I_{\mathrm{if}}(\mathbf{r}) = I_1(\mathbf{r}) + I_2(\mathbf{r}) + 2\sqrt{I_1(\mathbf{r}) I_2(\mathbf{r})}\, g^{(1)}(\mathbf{r}) \cos \Phi(\mathbf{r}) \,,$$

where $\mathbf{r}$ is the spatial coordinate and $\Phi(\mathbf{r})$ is the distribution of the phase difference between the interfering waves. The degree of coherence is determined by the absolute value of the normalized first-order correlator, $|g^{(1)}(\mathbf{r})|$, varying in the range from 0 (incoherent radiation) to 1 (coherent radiation). The correlator is directly related to the visibility of the interference fringes $V = (I_{\max} - I_{\min})/(I_{\max} + I_{\min})$. The dependence of $|g^{(1)}|$ on the coordinate x in the wavefront plane can be described by the function $\exp(-|x|/\xi)$. The transverse spatial coherence length $\xi \to 0$ for an incoherent light source and $\xi \to \infty$ for a coherent one. However, as already mentioned in Section 1, in a homogeneous two-dimensional gas of interacting bosons a BKT transition into a superconducting phase should occur, in which the decay of $|g^{(1)}(x)|$ follows a power law [30, 31]. Recently, for a condensate of intracavity exciton polaritons, a power-law decay of $g^{(1)}(x)$ was experimentally observed at distances up to ~ 40 μm [50].

In our experiments, a Michelson interferometer with a nonpolarizing beam-splitting cube and parallel beams was used, in one arm of which a 90°-prism, inverting the image, was installed instead of a mirror. The magnified image of the sample in the light of PRR, extracted from the cryostat with an optical window, was transferred to the input of the interferometer, where it was further additionally magnified. At the output, a cooled CCD camera recorded two superimposed images of the sample, rotated relative to each other by 180° and modulated by slightly curved interference fringes parallel to the edge of the prism. The fringe visibility $V(\delta)$ and the modulus of the correlator $|g^{(1)}(\delta)|$ symmetrically decay on both sides of the line corresponding to zero shift between the images, $\delta = 0$.

It is known that during image transfer by an ideal projection optical system, even in the case of an incoherent light source, the spatial distribution of the degree of coherence is not described by a delta function due to diffraction at the input aperture [49]. For a circular entrance pupil, the instrument function has the form $g^{(1)}(v) = 2J_1(v)/v$, where $J_1(v)$ is the Bessel function of the first kind and first order, $v = 2\pi\delta \sin\alpha/\lambda$, $\sin\alpha$ is the numerical aperture of the optical system, and λ is the wavelength of light. The position of the first zero of this function determines the optical resolution of the system [49]. The aperture of the short-focus ($f = 15$ mm) aspherical lens closest to the sample was $\sin\alpha \simeq 0.5$, i.e., the calculated resolution was $\simeq 1$ μm.

The spatial distribution of the correlator $g^{(1)}(\mathbf{r})$ was obtained by separately recording the intensity distributions for each arm of the interferometer $I_1(\mathbf{r})$, $I_2(\mathbf{r})$, the interferogram itself $I_{\text{if}}(\mathbf{r})$, and constructing on this basis the distribution $g^{(1)}(\mathbf{r})\cos\Phi(\mathbf{r})$. As a result of summing the intensity along the interference fringes, the profiles $I_{\text{if}}(\delta)$, $I_1(\delta)$ and $I_2(\delta)$ were obtained, from which the sign-varying function $g^{(1)}(\delta)\cos\Phi(\delta)$ was extracted, whose envelope is the desired dependence $g^{(1)}(\delta)$. The accuracy of its determination is improved upon taking to the modulus: $|g^{(1)}(\delta)\cos\Phi(\delta)|$.

For the analysis of the coherence properties of resonantly reflected light, a low-coherence (ideally incoherent) radiation source is required; therefore, the probe laser beam was focused onto the surface of a rotating ground glass, the image of which was projected onto the sample surface. The size of the probing spot on the sample was $\simeq 50$ μm, while the pump spot of size $\simeq 5$ μm was located at its center. To suppress the contribution to the interferogram from coherent radiation of the pump laser diode, the reflected beam was passed through an interference filter with a bandwidth of 10 nm. Measurement of the instrument function of the system in the reflected light of the probe laser was performed at the lowest temperature, $T = 0.55$ K, and in zero magnetic field, $B = 0$.

3. Experimental results and discussion

3.1 Photoinduced resonant reflection spectroscopy

In the PRR spectrum (Fig. 3), in accordance with the above discussion, a positive peak is observed in the region of the electronic (0–0) transitions and a negative peak in the region of the (1–1) transitions [25]. With increasing pump power density, the intensities of these peaks exhibit correlated behavior, which is caused by the formation of SCEs consisting of electrons of the first electronic Landau level $n_{\text{L}}^{\text{e}} = 1$ bound to Fermi holes of the zeroth electronic level $n_{\text{L}}^{\text{e}} = 0$ (Fig. 1a). From the registered maximum decrease in the resonant-reflection intensity for the (1–1) transition, it follows that the fraction of nonequilibrium SCEs excited in the dense ensemble of 2D electrons reaches 10–15% of the total number of electronic states in the Landau level N_{Φ}.

Figure 3 also presents the PL spectrum measured under the same conditions, demonstrating a circularly polarized σ^+–σ^--doublet corresponding to the electronic (0–0) transitions. The magnitude of the doublet splitting corresponds to the sum of the spin splittings in a magnetic field for the lowest cyclotron levels of heavy holes in the valence band $n_{\text{L}}^{\text{hh}} = 0$ and electrons in the conduction band $n_{\text{L}}^{\text{e}} = 0$.

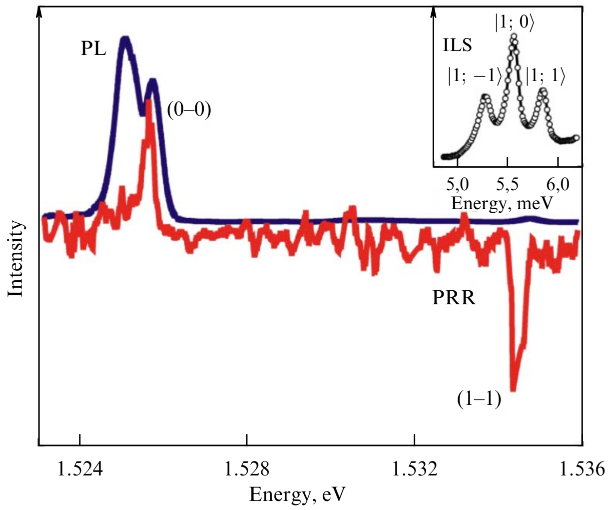

Figure 3. PL and PRR spectra at $\nu = 2$, measured in a 17-nm-wide GaAs/AlGaAs QW ($\mu_{\text{e}} \cong 5 \times 10^6$ cm^2 V^{-1} s^{-1}, $n_{\text{e}} \cong 2.4 \times 10^{11}$ cm^{-2}) in a magnetic field $B_{\perp} = 5$ T perpendicular to the QW plane at a temperature $T = 0.45$ K. The optical transition (0–0) occurs between the lowest cyclotron levels of conduction band electrons ($n_{\text{L}}^{\text{e}} = 0$) and valence band heavy holes ($n_{\text{L}}^{\text{hh}} = 0$), the transition (1–1) occurs between the first cyclotron levels: $n_{\text{L}}^{\text{e}} = 1$ and $n_{\text{L}}^{\text{hh}} = 1$. Inset: resonant ILS spectrum measured under the same experimental conditions and with a parallel magnetic field component $B_{\|} = 5$ T, introduced to enhance the Zeeman splitting of the spin components of the exciton triplet $|S; S_z\rangle$.

Even though triplet SCEs are not optically active, their existence can be directly established from the spectra of inelastic light scattering (see inset in Fig. 3), and these spectra can be used to determine the singlet-triplet exciton splitting [25, 51]. The singlet-triplet excitonic splitting is measured as the energy difference between the singlet exciton and the center of gravity of the excitonic triplet (the spectral position of the spin component with $S_z = 0$) observed in the spectra of inelastic light scattering. This splitting was found to be comparatively large, approximately 1 meV [25].

3.2 Lifetime of spin cyclotron excitons

The use of the PRR technique in the pulsed regime (see [25]) proved to be highly effective for investigating the relaxation times of SCEs, τ, as functions of temperature T, magnetic field B, quantum-well width, and, importantly, the quality of the heterostructures. The relaxation times of SCEs were found to be extraordinarily long: in the best structures they reach the millisecond scale [27]. The decay patterns of the PRR signal in the region of the optical (0–0) transitions for two quantum wells of different widths are presented in Fig. 4. It is seen that the kinetics are exponential, while the decay times τ amount to tens of microseconds. The rise kinetics of the PRR signal in the region of the (1–1) transitions occur on the same time scales, which indicates a common relaxation dynamic of the excitonic states formed from electrons on the first Landau level $n_{\text{L}}^{\text{e}} = 1$ and Fermi holes on the zeroth Landau level $n_{\text{L}}^{\text{e}} = 0$. This commonality also manifests itself in the temperature dependence of the relaxation rate presented in Fig. 5. At $T > 1$ K, the temperature dependence of the relaxation rate has an exponential form:

$$\tau^{-1}(T) = \tau_1^{-1} \exp\left(-\frac{\Delta}{k_{\text{B}}T}\right),$$

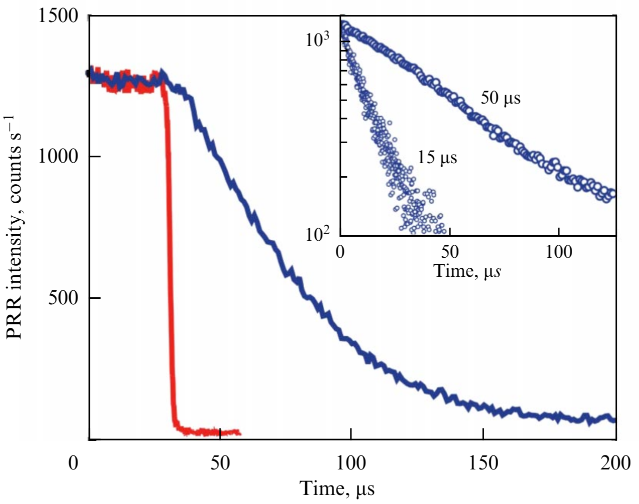

Figure 4. An example of the PRR decay kinetics (blue curve) and, for comparison, the instrumental function of the measuring system (red curve). Inset: the decay kinetics on a semi-logarithmic scale for 35-nm (long kinetics) and 17-nm (short kinetics) wide QWs at $\nu = 2$ in a field $B_\perp = 4$ T. Concentration $n_e = 2 \times 10^{11}$ cm^{-2}, mobilities $\mu_e = 15 \times 10^6$ cm^2 V^{-1} s^{-1} and $\mu_e = 5 \times 10^6$ cm^2 V^{-1} s^{-1}, respectively.

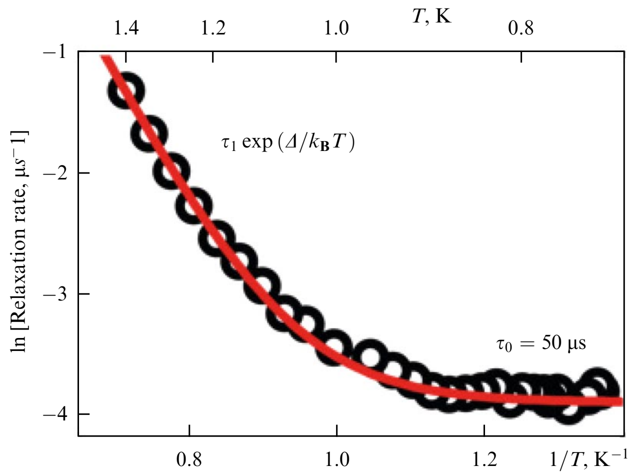

Figure 5. Behavior of the relaxation rate of triplet magnetoexcitons with changing temperature in a 35-nm-wide QW at $B_\perp = 4$ T. Circles represent the experiment, the solid line is a fit taking into account two relaxation mechanisms: activation and temperature-independent.

with a characteristic time $\tau_1 \approx 1$ ns and an activation gap $\Delta/k_B \approx 11$ K, where k_B is the Boltzmann constant. Such behavior means that in this temperature range there exists an activation relaxation channel involving electron spin-flip processes due to spin-orbit interaction, an increase of the exciton energy to the cyclotron energy, and subsequent emission of a photon with cyclotron energy [19]. The measured activation gap is nothing other than the Coulomb binding energy of the triplet exciton, equal to the energy of the singlet-triplet excitonic splitting, which, in turn, can be independently measured from the spectra of inelastic light scattering. In the range $T \leqslant 1$ K, the decay time of the PRR signal ceases to depend on temperature: $\tau = \tau_0$ (Fig. 5). In this temperature range, a change in the relaxation mechanism occurs, and this mechanism is no longer thermally activated.

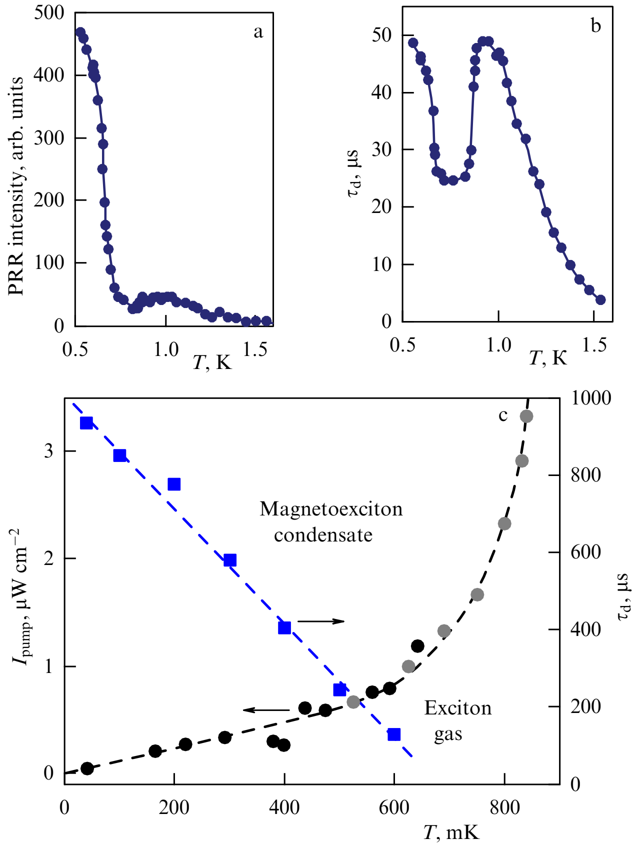

Figure 6. Temperature dependences of: (a) the PRR signal intensity and (b) its decay time $\tau_d(T)$ for SCEs under steady-state photoexcitation conditions at a pump intensity $I_{pump} \approx 30$ mW cm^{-2}. (c) Phase boundary separating the regions of existence of the incoherent gas and the SCE condensate. Points represent the experiment (gray circles from Ref. [26], black circles from Ref. [45]). The black dashed line is guided for the eye. Blue squares and the dashed line show the result of measurements of the temperature dependence of the PRR signal decay time $\tau_d(T)$ — right axis.

3.3 Magnetoexciton condensate. Phase transition

The discovered long lifetimes of SCEs in the 2DES, record-breaking for translationally invariant systems, opened a unique opportunity for studying a degenerate Fermi system in which a dense ensemble of long-lived spin-flip excitons obeying Bose statistics is excited by light. Figures 6a and 6b present the results of measurements of the temperature dependence of the PRR signal intensity $I_{PRR}(T)$ and its decay time $\tau_d(T)$ upon smooth lowering of the temperature T and at a fixed optical pumping power ($I_{pump} \approx 30$ mW cm^{-2}), creating an SCE density $N_{ex} \sim 10^{10}$ cm^{-2}. It was found that in the region $T \leqslant 0.8$ K, I_{PRR} sharply increases by more than an order of magnitude (Fig. 6a), whereas the time τ_d sharply decreases (Fig. 6b). The threshold-like character of these phenomena suggests the emergence of a new condensed SCE phase. It is difficult to imagine that a change in the temperature of the excitonic ensemble by only 0.1 K could radically alter the mechanism of exciton relaxation. A much more realistic assumption is the threshold acceleration of exciton spreading from the pumping/probing spot region (see the next section). The threshold temperature T_c corresponding to the jump in I_{PRR} is sensitive to the optical pumping intensity: upon decreasing I_{pump} it shifts toward lower temperatures. Measurement of the threshold for the increase of the PRR signal as a function of temperature and pumping made it possible to construct, in the temperature range

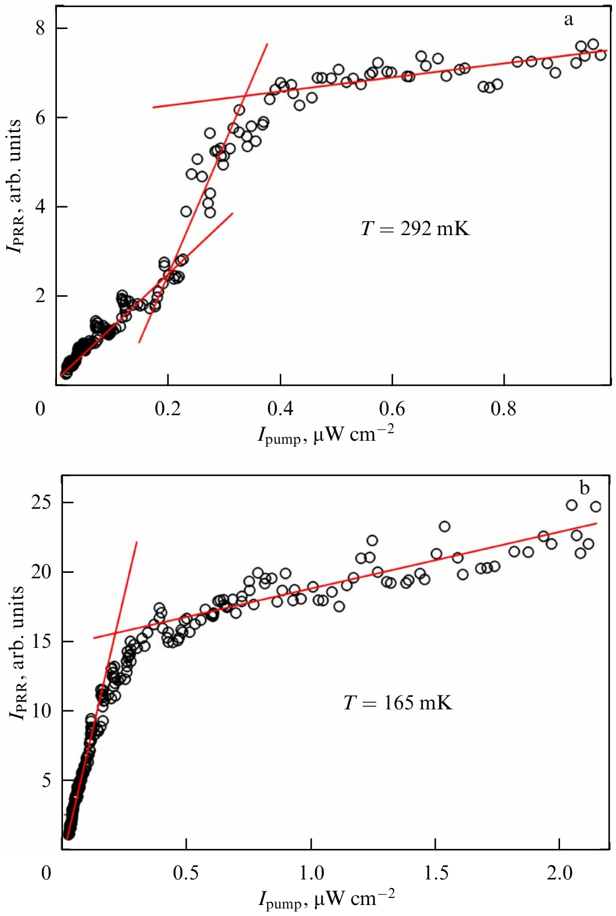

Figure 7. Dependence of the PRR signal intensity I_{PRR} on the pump power density I_{pump} at helium bath temperatures $T = 292$ mK (a) and $T = 165$ mK (b).

$0.53\ \mathrm{K} \leqslant T \leqslant 0.85$ K, a phase diagram in the '$T - I_{\mathrm{pump}}$' coordinates (gray points in Fig. 6c) with a boundary separating the regions of existence of the magnetoexciton gas and a new, denser condensed SCE phase, which hereafter will be referred to as the *magnetoexciton* (*magnetofermionic*) condensate [27]. The threshold for the emergence of the new excitonic phase was determined from the critical temperature T_{c}, corresponding to one-half of the step height observed for the parameter $f(T) = I_{\mathrm{PRR}}(T)/\tau_{\mathrm{d}}(T)$, proportional to the oscillator strength of the optical transition (0–0).

In the temperature range $0.04\ \mathrm{K} \leqslant T \leqslant 0.6$ K, the 'gas–SCE condensate' transition diagram in the '$T - I_{\mathrm{pump}}$' coordinates was constructed using measurements of the dependence of the PRR signal amplitude I_{PRR} on the photogeneration power density I_{pump} at various fixed helium bath temperatures and constant intensity of the probing resonant laser radiation [52]. At low pumping powers, $I_{\mathrm{PRR}}(I_{\mathrm{pump}})$ grows linearly due to the linear increase in the number of SCEs. In the vicinity of the 'gas–condensate' transition, an effect of nonlinear enhancement may be observed (Fig. 7a), which weakens with decreasing temperature and is no longer observed at $T \lesssim 400$ K (Fig. 7b). On the other hand, throughout the entire investigated temperature range, a clearly pronounced decrease in the growth rate of the PRR signal with pumping is observed in the dependence $I_{\mathrm{PRR}}(I_{\mathrm{pump}})$ (Fig. 7). Such behavior is naturally associated with the 'gas–condensate' transition, as a result of which rapid spreading of the SCEs from the pumping region and the PRR signal detection region begins. When constructing the 'gas–condensate' transition diagram in the '$T - I_{\mathrm{pump}}$' coordinates, the transition point was taken to be the value of the power density $I^{\mathrm{o}}_{\mathrm{pump}}$, corresponding to the kink in the dependence $I_{\mathrm{PRR}}(I_{\mathrm{pump}})$, if it is approximated by two straight lines (see Fig. 7). The obtained results are shown in Fig. 6c (black points).

At $T \lesssim 500$ mK, the dependence of the photogeneration power density on temperature at the 'gas–condensate' transition boundary, $I^{\mathrm{o}}_{\mathrm{pump}}(T)$, is close to linear; however, at higher temperatures a strong superlinear growth is observed. Moreover, already at $T \gtrsim 1$ K, it is impossible to reach the 'gas–condensate' transition boundary. Evidently, with increasing temperature, the 'lifetime' of SCEs in the photogeneration spot decreases so rapidly that increasing their generation rate by increasing I_{pump} does not compensate for the decrease in the quasiequilibrium density of SCEs in the photogeneration spot.

The phase diagram in the '$T - I_{\mathrm{pump}}$' coordinates provide an understanding of the experimental possibilities for obtaining a magnetoexciton condensate, but does not allow one to understand the temperature dependence of the critical SCE density $N_{\mathrm{ex}}(T)$ required for condensation. The region of the phase diagram in Fig. 6c denoted as the 'magnetoexciton condensate' shows only the variation of the SCE density excited within the pumping spot. At the same time, an increase in the power density I_{pump} may not affect the *quasistationary* SCE density in the condensate, N_{ex}, since the entire 'excess' density of quasiequilibrium SCEs may spread beyond the photogeneration spot or relax to the ground state and therefore make no contribution to the PRR signal. A physically correct phase diagram of the 'gas–condensate' transition should be constructed in the 'temperature–quasistationary SCE density N_{ex}' coordinates.

The quasi-stationary SCE density N_{ex} within the excitation spot under continuous optical pumping is proportional to the product of the pumping power density I_{pump} and the time τ_{d}, irrespective of whether this time is determined by exciton relaxation to the ground state or by spreading beyond the pumping/probing spot. The 'gas–condensate' transition diagram constructed in the '$T - I_{\mathrm{pump}}\tau_{\mathrm{d}}$' coordinates reflect the actual dependence of the phase boundary on the quasistationary SCE density N_{ex}. It was found that, within the experimental uncertainty, the position of the phase boundary in the '$T - N_{\mathrm{ex}}$' diagram does not depend on temperature (Fig. 8). Thus, it may be concluded that the magnetoexciton SCE condensate represents an incompressible state in real space, while the condensate density, within the available experimental accuracy, does not depend on temperature.

Unfortunately, there exists no exact method for determining the absolute value of the SCE density at the 'gas–condensate' transition boundary analogous to magnetotransport measurements of the Hall conductivity [53]. Therefore, at present it is impossible to specify the absolute value of N_{ex} required for their condensation. A theoretical estimate of this density obtained in Ref. [54] amounts to 5–10% of the magnetic flux quantum density N_{Φ}. Independent photoluminescence studies of the two-dimensional electron gas allow one to conclude that at a Fermi-hole density exceeding $0.15 N_{\Phi}$, the SCEs become unstable [27]. Therefore, the estimate of the SCE density $N^{\mathrm{o}}_{\mathrm{ex}}$ required for condensate formation in the range $N^{\mathrm{o}}_{\mathrm{ex}} = (0.05 - 0.15) N_{\Phi}$ appears reasonable. The search for a method to improve the accuracy of this estimate is one of the future problems in the physics of the

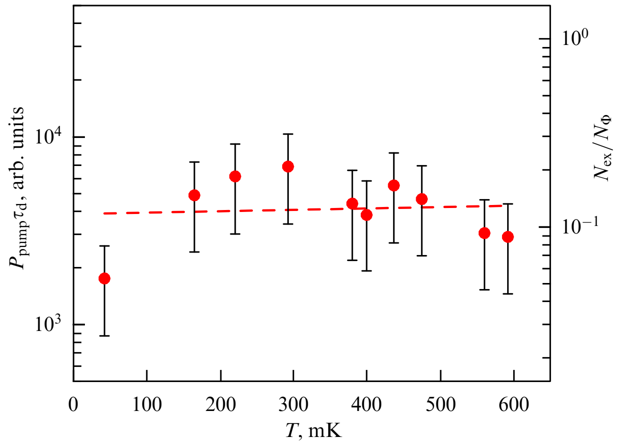

Figure 8. Phase diagram of the 'gas–magnetoexciton' condensate transition in the '$T-N_{\rm ex}$' coordinates. The left scale shows the values of the experimental data $P_{\rm pump}\tau_{\rm d}$ describing the quasi-steady-state density of SCEs in the excitation spot. The right scale shows the $N_{\rm ex}$ values corresponding to theoretical estimates [26, 55].

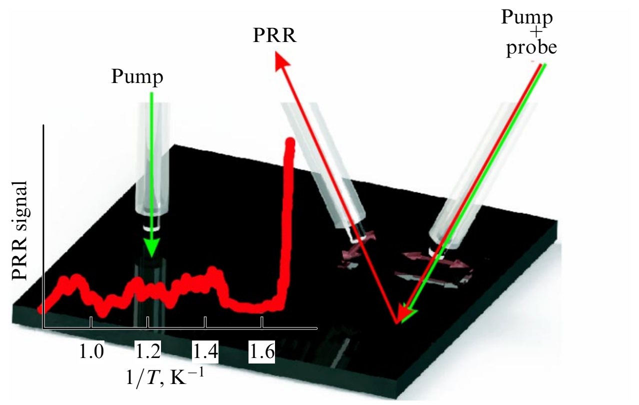

Figure 9. Schematic of the PRR measurement experiments. Standard two-fiber schematic for PRR registration (right) and an additional pump fiber for spatially resolved PRR measurements (left). Inset: temperature dependence of the PRR signal registered at a distance of ≈ 2 mm from the pump spot.

magnetoexciton condensate. The phase diagram itself in the '$T-N_{\rm ex}$' coordinates consists of two extensive regions: the region of the magnetoexciton gas, $N_{\rm ex} < N_{\rm ex}^{\rm o}$, and the region of the gas of uncorrelated excited electrons, $N_{\rm ex} > N_{\rm ex}^{\rm o}$, in which the SCEs are unstable. These regions are separated by the condensate line, $N_{\rm ex} = N_{\rm ex}^{\rm o}$, possibly broadened due to fluctuations of the random potential of the quantum well [54].

3.4 Magnetoexciton condensate. Spreading

The hypothesis of a rapid spreading of the magnetoexciton condensate from the photoexcitation spot was experimentally verified using a spatial separation of the optical fibers employed for the excitation and detection of SCEs (Fig. 9) [27]. For delivering the optical pumping radiation, an additional third optical fiber was used, brought as close as possible to the sample, i.e., the photoexcitation spot size was ≈ 0.4 mm. A pair of optical fibers for measuring the PRR amplitude was positioned at a distance of ≈ 2 mm. At $T > 1$ K, the PRR signal for the electronic transition (0–0) remained small and was lost in the noise. A decrease in temperature to $T \lesssim 0.75$ K led to a sharp increase in the signal. This implies that a significant number of photoexcited SCEs, under conditions of their condensation in the fermionic 2DES, spread out of the excitation region over macroscopically large distances in a nondiffusive manner.

The spreading of the magnetoexciton condensate was visualized using a cryostat with an optical window, allowing the sample to be observed in the light of PL or resonant reflection [55]. For recording the PRR pattern, a wide probe laser spot ($\gtrsim 200$ μm) was used. The pump spot of size ≈ 10 μm was located inside the probe spot and was visualized in the light of PL corresponding to the optically allowed transition (0–0). The corresponding recombination time is ~ 100 ps, and the size of the luminescence spot remains constant at any investigated temperature (Fig. 10a). Taking into account the spatial resolution of the optical system, the diffusion length in the spin exciton gas did not exceed 2 μm. No escape of SCEs from the excitation spot is observed as long as their density is below the critical value for the formation of a magnetoexciton condensate. When the phase transition into the condensed state occurs, the propagation lengths of SCEs from the excitation spot become

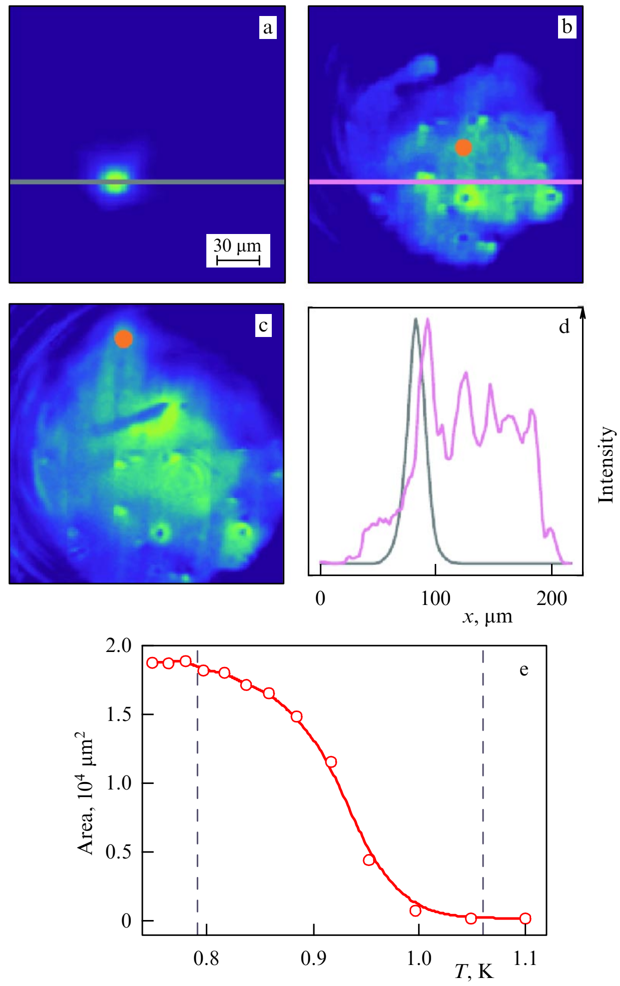

Figure 10. Propagation of SCEs over macroscopic distances. (a) Photoexcitation spot observed in PL light — optical transition (0–0). (b) and (c) images in PRR light of the same sample area at different positions of the excitation spot (orange circle). d) Intensity profiles of PL and PRR along the lines shown in (a) and (b). $T \approx 0.5$ K, $I_{\rm pump} = 80$ mW cm^{-2}. (e) Temperature dependence of the SCE spreading area. The phase transition to the magnetoexciton condensate occurs between the two dashed lines.

macroscopic (Figs 10b, c). The distance over which spin-flip excitons spread across the sample increases with the excitation spot size and with the pump power. In Fig. 10c, the propagation length of SCEs exceeds 200 μm at a pump spot diameter of 20 μm. The spatial distribution of SCEs from the edge of the photoexcitation spot to the front of their propagation is not described by a Gaussian distribution. Instead, a plateau of SCE density is observed, with dips due to the presence of defects in the investigated heterostructure (Fig. 10d). Thus, the transport of spin-flip excitons is not a diffusive process. By varying the temperature within a narrow range of ~ 0.2 K, one can either completely suppress their propagation or allow it over a certain distance (Fig. 10e).

Another method for diagnosing the spreading of the magnetoexciton condensate is related to the 'signal markers' of SCEs mentioned in Section 2.2.2, which are observed in the PL spectra. In experiments [56], the beam of the 2DES excitation source was split into two: a pumping beam and a probing beam. Both beams were focused on the sample surface into spots with a diameter of ≈ 20 μm, separated by a distance of ≈ 200 μm. The pump power P_{pump} was varied in the range from 2 to 200 μW, while the power of the probe beam was maintained constant: $P_{\text{probe}} = 3$ μW. The concentration of dark SCEs in the pump spot could be changed by varying P_{pump}. The arrival of SCEs at the probe spot was detected by the PL spectrum. Spectrum (2) in Fig. 2 was measured in the absence of pumping in the photoexcitation spot. It shows two lines corresponding to single-particle transitions, as well as relatively weak lines 'Pln' and 'T' arising due to the presence of a small number of SCEs in the probe region, which are generated by the probe beam itself. At a low pumping level in the photoexcitation spot, $P_{\text{pump}} < 6$ μW, the shape and intensity of the PL spectrum in the probe spot remained practically unchanged. That is, under these conditions, the ensemble of SCEs created in the photoexcitation spot exerts practically no influence on the states in the probe spot. However, with an increase in the pumping intensity in the excitation spot, the 'Pln' and 'T' lines associated with optical transitions in many-particle complexes grow in intensity and become dominant in the probe spot (spectrum (3) in Fig. 2). From here it unambiguously follows that at a sufficient pump power, SCEs from the photoexcitation spot arrive at the probe region, overcoming a distance of ~ 200 μm.

After obtaining such detailed information about the transport properties of SCEs in a quantum Hall insulator at $\nu = 2$, comparative studies were carried out on a new, recently discovered condensed state consisting of spin-magnetogravitons in a Laughlin liquid at $\nu = 1/3$ [38–41]. Some properties of this new type of condensate are equivalent to the properties of the SCE condensate at $\nu = 2$, namely: the spin quantum number, momentum, and ultra-large relaxation times of excitations. However, despite the similarity, the transport characteristics of excitations at the filling factor $\nu = 1/3$ are completely different. Practically, with an increase in the concentration of excitations by two orders of magnitude — from the single-particle limit to the maximum possible saturation level of the Laughlin liquid with spin-magnetogravitons — no spreading in real space is observed (see Fig. 11). Given such a striking contrast in the transport properties of magnetoexcitations with spin 1 observed in the bulk of integer and fractional quantum Hall insulators, and taking into account the collective nature of SCE transport in real space, it made sense to compare the spatial coherence of dense ensembles of excitations in these two cases.

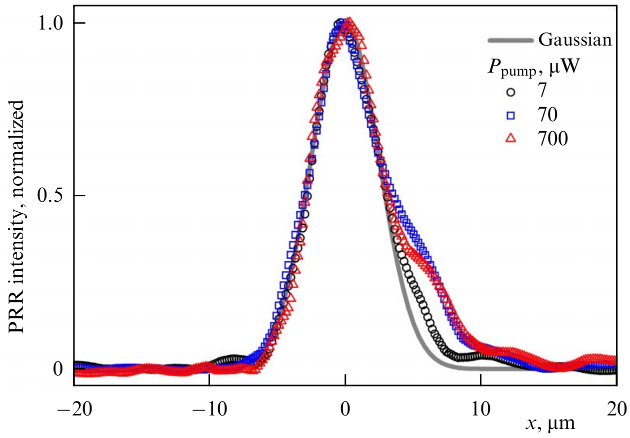

Figure 11. Spatial distribution profile of the PRR signal from the photoexcitation region of a fractional quantum Hall insulator ($\nu = 1/3$). Points represent measurement results at the indicated pump powers. The gray curve is a Gaussian distribution profile with a radius of 5 μm. $T \approx 0.55$ K.

3.4.1 Kinetics of spreading of spin excitons. The kinetics of the spreading of SCEs was investigated using a two-fiber technique [57–59]. Modulation of the current of a single-mode laser diode ($\lambda \approx 780$ nm) using a square-pulse generator allowed the measurement of τ_{d}, the decay time of the PRR signal from the photoexcitation spot after the end of the pump pulse. An increase in the pump pulse duration t_{p} or the peak power P_{p} led to an increase in the density of SCEs pumped per pulse. The pulse repetition period T_{p} was chosen to exceed all characteristic transient and relaxation processes in the investigated system and amounted to tens of milliseconds. It should be noted that in these measurements it is impossible to determine due to what the PRR signal decays after the end of the pump pulse. This can be related both to the relaxation of nonequilibrium SCEs into the ground state in a time τ and to their escape from the photoexcitation spot in a time τ_{prop}. In both cases, a decrease in the number of Fermi holes comprising the SCEs is recorded in the pump/probe spot.

The results of measurements of the PRR signal decay time τ_{d} as a function of the pump pulse duration t_{p} at a fixed peak power P_{p} are shown in Fig. 12. Three characteristic regions can be distinguished on the curve. In the first region, at a low photoexcitation level, the concentration of SCEs is less than 1% of the magnetic flux quantum density, and the decay time weakly depends on the duration of the photoexcitation pulse: $\tau_{\text{d}} \approx 600$ μs. In the second region, an increase in τ_{d} by approximately 300 μs is observed, and in the third region, a sharp drop occurs.

A disadvantage of the PRR method is that only the total number of photoexcited Fermi holes is recorded, and it is unknown what generalized momentum is possessed by the SCEs of which these holes are part. To understand the behavior of spin-flip excitons in the photoexcitation spot depending on the pumped exciton density, simultaneous measurements of the PL spectra of the 2DES were performed [59]. In the insets in Fig. 12, it is seen that at low photoexcitation densities, the number of SCEs with large generalized momenta is small: the plasmaron line is absent. With increasing exciton density, the process of scattering of light-generated SCEs with momenta $q \approx 0$ into the region of the dispersion minimum begins — the plasmaron line with

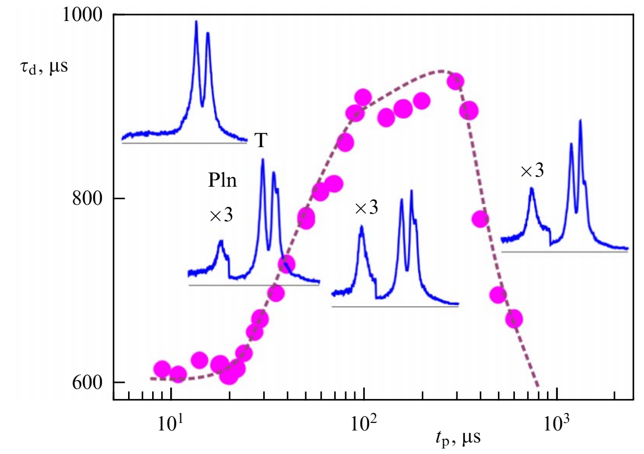

Figure 12. PRR signal decay time as a function of the photoexcitation pulse duration $\tau_d(t_p)$. Insets show PL spectra measured at $t_p = 10, 30, 100$, and 1000 μs.

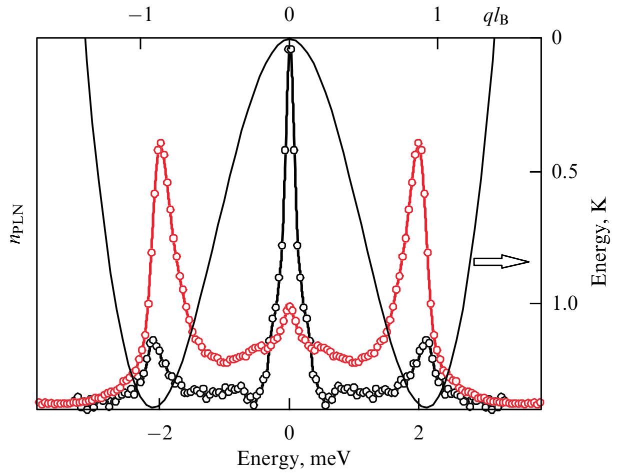

Figure 13. Distribution of plasmarons over energies (bottom scale) and momenta (top scale) for two continuous-wave photoexcitation regimes corresponding to spectra (*2*) (black curve) and (*3*) (red curve) in Fig. 2. The thin line indicates the dispersion of triplet magnetoexcitons calculated in accordance with the results of [22].

SCE momenta $q \approx 1/l_B$ grows faster than the trion line. This process begins from a certain critical pump pulse duration, i.e., from a critical density of SCEs. It is natural to assume that spin-flip excitons do not have enough time during their lifetime to thermalize and fill the energy states near the minimum of the dispersion relation. The reason for the slow intravalley relaxation is the impossibility of simultaneously satisfying the energy and momentum conservation laws during the emission of an acoustic phonon. The specific values of the relaxation time are related to the parameters of the heterostructure. In our case, a lower bound for this time is at least 600 μs.

The process of SCE scattering into the lowest energy state is accompanied by the appearance of the plasmaron line in the PL spectra, which signals the filling of magnetoexciton states near the minimum of the dispersion relation. At the same time, the relaxation time of SCEs into the ground state, measured using PRR, increases (the second region in the dependence $\tau_d(t_p)$, Fig. 12). This is an obvious result, since in the process of relaxation into the ground state, spin-flip excitons must, in addition to energy, transfer a large momentum $q \approx 1/l_B$. The most interesting is the behavior of the PL spectra in the regime where SCEs begin to escape from the excitation spot. In this case, the time τ_d sharply decreases. Simultaneously, an imbalance is observed between the total number of SCEs pumped in the excitation spot, to which the intensity of the trion line is proportional, and the number of SCEs with the generalized momentum $q \approx 1/l_B$, measured using the plasmaron line. If the former number grows, the latter decreases. Obviously, not all photoexcited SCEs have time to escape from the excitation spot, but mainly excitons with the generalized momentum $q \approx 1/l_B$. The velocity they acquire upon escaping from the pump spot can be roughly estimated as $v_c \approx d_{pump}/2\tau_{prop}$ The minimum time τ_d recorded in the experiments was ≈ 30 μs [57, 58], which gives an estimate for the maximum spreading velocity of ≈ 25 m s^{-1}.

In experiments with spatially separated pump and probe spots, it is observed that with increasing photoexcitation power density, the intensity of the plasmaron line in the remote region grows until it approaches the integrated intensity of the trion line. This means that practically all SCEs that have arrived at the detection region from the excitation spot possess the generalized momentum $q \approx 1/l_B$. By subtracting with an appropriate weight the PL spectrum of the equilibrium 2DES from the PL spectra in the remote region, one can obtain the generalized momentum distribution of nonequilibrium SCEs [59]. From the distribution functions $n_{SCE}(q)$ shown in Fig. 13, with and without the remote photoexcitation, it is seen that it is the SCEs with momenta $q \approx 1/l_B$ that take part in the magnetoexciton transport.

Due to the impossibility of simultaneously satisfying the energy and momentum conservation laws, complete thermalization does not occur in the SCE ensemble. Relaxation into the lowest energy state proceeds via two-exciton processes [60], which become noticeable when the SCE ensemble reaches a certain critical density. Due to ultra-long thermalization times, the SCE ensemble is essentially nonequilibrium. One part of it represents a gas of magnetoexcitons with generalized momenta $q \approx 0$. Their fraction is determined not only by the temperature, but also by the photoexcitation dynamics, two-exciton intravalley relaxation, and the transport of SCEs out of the pump spot. The other part consists of SCEs with momenta $q \approx 1/l_B$, which form the magnetoexciton condensate and spread over macroscopic distances.

3.4.2 Features of spreading of the magnetoexciton condensate. Interesting, finer features of SCE spreading were discovered as a result of improving its visualization methods [61–63]. The high spatial coherence of the probe laser makes it difficult to observe the sample in the light of PRR due to parasitic interference and speckle structure. To reduce the degree of coherence, the probe laser beam was focused onto the surface of a rotating ground glass into a spot, the image of which was projected onto the sample surface. In recent visualization experiments, a high-aperture projection optical system with high spatial resolution and precise focusing was used.

In the example shown in Fig. 14, the size of the photoexcitation region (PL spot) is ≈ 30 μm (Fig. 14a). Upon spectral recording of the PRR signal $I_{PRR}(\lambda)$ and tuning the probe laser wavelength to the maximum ($\lambda = \lambda_{max}$), a regular bright circular spot with a diameter of ≈ 40 μm is observed (Fig. 14b). With increasing pump power P_{pump}, the spot size can increase by a factor of 2–3, but no

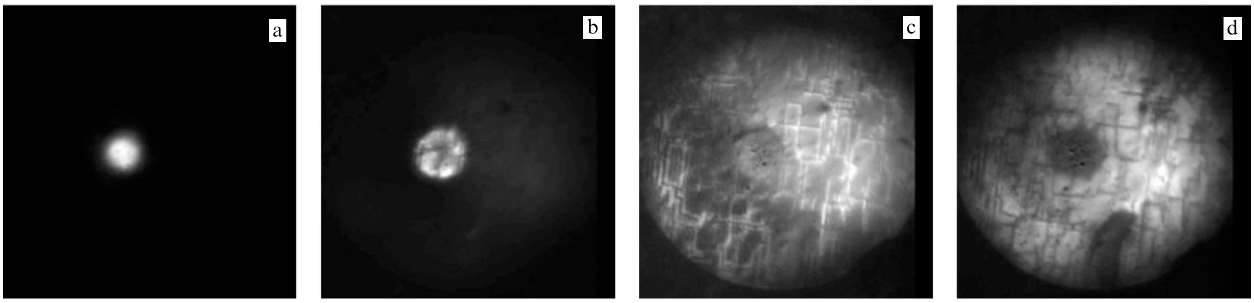

Figure 14. Image of the sample: (a) in photoluminescence light and in resonant reflection light at wavelengths (b) $\lambda_{\max}$, (c) $\lambda_1 \approx (\lambda_{\max} - 0.1$ nm), and (d) $\lambda_2 \approx (\lambda_{\max} - 0.2$ nm) (see text). The frame side size is ≈ 310 μm. $P_{\text{pump}} = 10$ μW. $T \approx 0.55$ K.

more. The pattern changes drastically upon a smooth tuning of the probe laser to the blue side from $\lambda_{\max}$: the brightness of the central spot decreases, it becomes more uniform, and a less bright pattern, dissected by a grid of bright thin lines oriented perpendicular to each other, lights up around it over the entire field of view (in this case ≈ 350 μm) (Fig. 14c). At some point, when a certain wavelength $\lambda = \lambda_2$ is reached, the brightness of the reflection pattern at the periphery becomes maximum, and the contrast of the grid of lines reverses: now they are dark against a light background. The spot in the center also appears darker (Fig. 14d). With a further decrease in the wavelength, the entire PRR pattern gradually fades out. Due to the sample inhomogeneity, the value of λ_2 varies, remaining smaller than $\lambda_{\max}$ by 0.1–0.3 nm. The wavelength $\lambda_{\max}$ practically coincides with the position of the trion line in the PL spectrum: a very small blue shift is possible. It should be noted that not two, but three or even four resonances can be observed in the PRR spectrum $I_{\text{PRR}}(\lambda)$, but only in one of them, at $\lambda = \lambda_2$, is spreading over the entire field of view observed. In the remaining resonances, the pattern is qualitatively close to the case of $\lambda = \lambda_{\max}$. As for the intensity of the resonances, at $\lambda = \lambda_{\max}$ the resonance is always the strongest and exceeds the intensity of the resonance at $\lambda = \lambda_2$ by one to two orders of magnitude.

Why is the size of the bright reflection region around the pump spot limited to tens of microns at the wavelength $\lambda_{\max}$, whereas a much larger area, limited by the field of view of the optical system, is illuminated upon a small detuning toward shorter wavelengths? The answer is related to the conclusion of the previous section: the ensemble of light-generated triplet cyclotron magnetoexcitons consists of SCEs with momenta $q \simeq 0$ and those SCEs that fill the energy minimum near $q_{\min} \approx 1/l_{\text{B}}$ and carry out spin transport, practically, over the entire sample. It follows from the results in Fig. 14 that using PRR at the wavelength $\lambda_{\max}$, only SCEs with a small value of q are recorded, which turn out to be capable of propagating in space over much smaller distances. Upon spectral recording of $I_{\text{PRR}}(\lambda)$, the most intense resonance maximum is obtained when detecting the PRR signal from SCEs concentrated in a small region around the pump spot. A shift toward smaller λ detects SCEs that have condensed in the energy minimum, which rapidly spread over macroscopic distances and fill the entire field of view.

Why this occurs precisely at a blue shift can be understood on a qualitative level from Fig. 15. The point is that a Fermi hole at the zeroth Landau level is described by an *s*-type wavefunction, whereas an excited electron at the first Landau level is described by a *p*-type wavefunction. As a consequence, the overlap integral and, accordingly, the binding energy of

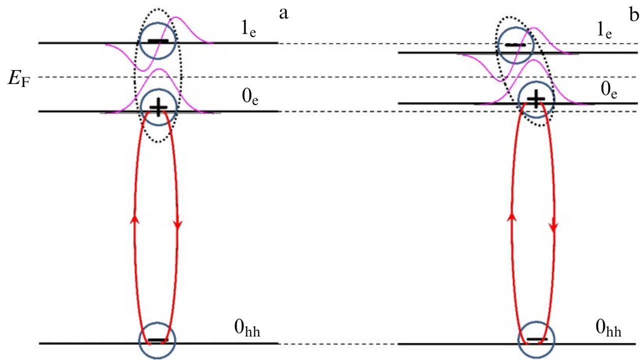

Figure 15. Schematic of the overlap of wave functions (purple lines) and energy levels of a Fermi hole at the lowest electronic Landau level and an excited electron at the first level, as well as optical transitions (0–0) during the detection of a Fermi hole using resonant light reflection (red lines): (a) for triplet magnetoexcitons with a generalized momentum $q \approx 0$ and (b) $q \approx 1/l_{\text{B}}$.

the electron and the Fermi hole in an SCE with a generalized momentum $q \simeq 0$ (Fig. 15a) are smaller than those of an exciton with $q \simeq 1/l_{\text{B}}$ (Fig. 15b). As a result, the energy levels of the excited electron at the first Landau level and the Fermi hole at the zeroth Landau level are 'attracted' to the Fermi level somewhat closer for a magnetoexciton with $q \simeq 1/l_{\text{B}}$ than for a magnetoexciton with $q \simeq 0$. Therefore, the energy of a photon detecting a Fermi hole in an SCE with $q \simeq 1/l_{\text{B}}$ using PRR is somewhat higher than that of a photon detecting a Fermi hole with $q \simeq 0$.

It follows from the obtained results that SCEs with a small value of q also propagate in space in a far from trivial manner. Their spatial distribution also has nothing to do with diffusion and is described by a step function, and the diameter of the uniform plateau exceeds the mean free path of an individual SCE with $q \approx 0$ in the gas phase by two orders of magnitude [27]. Thus, it can be assumed that at small momenta as well, the spreading of SCEs has a collective nature. This observation qualitatively confirms the theoretical statement made in [54] that at $\nu = 2$, two types of condensed states should exist: one of which is formed from SCEs with $q \approx 0$, and the second is a condensate at $q \simeq 1/l_{\text{B}}$.

3.5 Coherence of the magnetoexciton condensate

In the study of the spatial coherence of the magnetoexciton condensate [64, 65], interferograms in the light of resonant reflection for the optical transition (0–0) between the states of the zeroth Landau levels of valence-band heavy holes and conduction-band electrons, obtained without optical pumping and with the pump switched on, were compared. In an

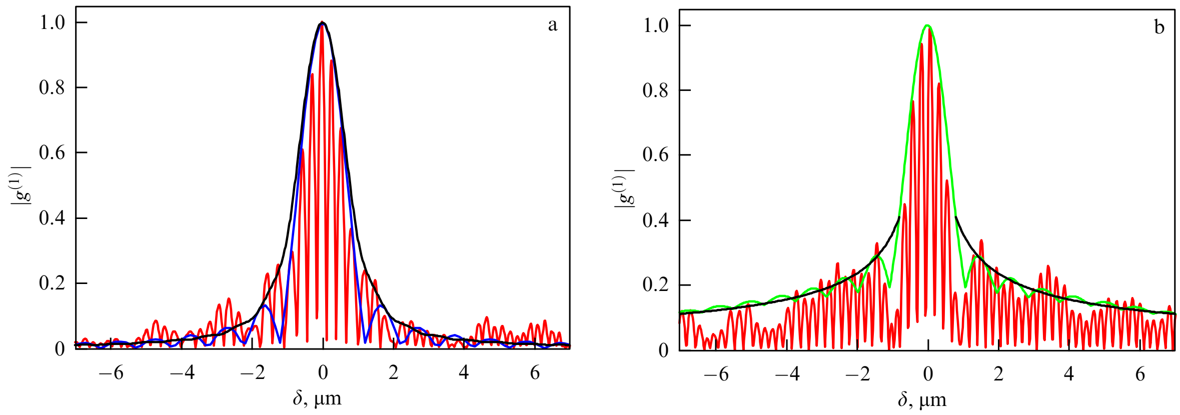

Figure 16. Estimation of the degree of coherence of the magnetoexciton condensate. The red line is the profile of interference fringes in resonant reflection light $|g^{(1)}(\delta)\cos\Phi(\delta)|$. (a) $P_{\rm pump} = 0$, $P_{\rm probe} = 5$ μW; the blue line is the instrumental function $|2J_1(v)/v|$ that best describes the central peak; the black line is the result of its convolution with the function $\exp(-|\delta|/\xi)$ at $\xi = 0.4$ μm. (b) $P_{\rm pump} = P_{\rm probe} = 1$ μW; the green curve is the result of summation with weights of 0.8 and 0.2, respectively, of the instrumental function and its convolution with $\exp(-|\delta|/\xi)$ at $\xi = 10$ μm; the black curve is the function $(0.18/|\delta|)^{0.6}$.

ideal 2D electron system, in the absence of photoexcitation, the resonant reflection signal from a quantum Hall insulator at $v = 2$ should not be observed: the absorption of a resonant photon and its subsequent re-emission (i.e., resonant reflection) is impossible until a Fermi hole appears at the zeroth electron Landau level. In reality, crossed linear polarizers do not suppress the reflection completely, and a certain amount of light enters the interferometer. Switching on the pump leads to the emergence of the PRR signal (the reflection increases by at least an order of magnitude), which indicates the appearance of a macroscopic number of nonequilibrium SCEs in the 2DES. The maximum intensity of the plasmaron band peak at $q_{\rm min} \approx 1/l_{\rm B}$ relative to the trion line served as a criterion for the formation of the magnetoexciton condensate during the adjustment of experimental parameters: the magnetic field strength B and the pump power $P_{\rm pump}$. It was found that the intensity of the 'Pln' line becomes comparable to the 'T' line, and the line of the single-particle transition, observed, like the plasmaron, in σ^--polarization, practically disappears at a pump intensity $I_{\rm pump} \lesssim 10$ W cm^{-2} and a filling factor $v \gtrsim 2$. The PL spectrum with an intense plasmaron line was recorded immediately before the registration of the interferogram and monitored after. The profile $|g^{(1)}(\delta)\cos\Phi(\delta)|$ in the absence of photoexcitation is shown in Fig. 16a, and with the pump switched on — in Fig. 16b.

In Figure 16a, the instrumental function that best describes the central peak at $\delta = 0$ is shown in blue. The result of the convolution of the instrumental curve and the function $\exp(-|\delta|/\xi)$ with the parameter $\xi = 0.4$ μm is also presented here. Obviously, the high degree of coherence of the probe laser radiation is not completely lost upon scattering by the ground glass. In any case, the first zero of the function $|2J_1(v)/v|$ in the fringe profile is clearly not observed, and the convolution result is closer to the experiment.

The widths of the central peaks in Figs. 16a and 16b differ little. The main difference lies in the behavior of $|g^{(1)}(\delta)|$ at large shifts. Although the reproducibility of $|g^{(1)}(\delta)|$ from measurement to measurement in this region of δ leaves much to be desired, the growth of the 'wings' of the $|g^{(1)}(\delta)|$ distribution when the pump is switched on is reliably reproduced. Figure 16b shows an example where this effect is maximal. The dependence $|g^{(1)}(\delta)|$ in Fig. 16b cannot be obtained by any convolution of $\exp(-|x|/\xi)$ with the instrumental function: with such a width of the central peak, the decay of the correlator with distance would occur much faster. Qualitatively, the pattern is explained under the assumption that there are two independent radiation sources: an incoherent one ($\xi \lesssim 0.1$ μm) and a partially coherent one with the parameter $\xi \sim 10$ μm (it is impossible to determine more precisely here). The result of summing the instrumental function and its convolution with the exponential $\exp(-|\delta|/\xi)$ at $\xi = 10$ μm with weights of 0.8 and 0.2, respectively, is shown in Fig. 16b by the green curve.

The dependence $|g^{(1)}(\delta)|$ in Fig. 16b is very similar to that first observed for intracavity exciton polaritons in [50]. In that case, the central peak was well described by a Gaussian, the width of which is directly related to the thermal de Broglie wavelength $\lambda_{\rm dB}$, reaching 5–6 μm at a high optical pump intensity. The mass of the SCE is much larger ($m_{\rm SCE} \approx 0.13 m_{\rm e}$); therefore, for it at $T = 0.5$ K $\lambda_{\rm dB} \approx 0.3$ μm. Since the resolution of our optical system is no better than 1 μm, it is precisely what determines the peak width at $\delta \simeq 0$. The behavior of the correlator at large distances can also be described by a power-law dependence of the form $(b/|\delta|)^a$, which should be observed at the BKT transition: the black curve in Fig. 16b. The accuracy of determining the exponent is small, but it can still be argued that $a \simeq 0.5-0.7$. According to the BKT theory, in a condensate of 2D bosons, the value of the exponent obeys the condition $a \leqslant 1/4$ [29, 30]. In experiments [50], where the measurement accuracy is much higher, values of $a \simeq 0.9-1.2$ were obtained. Subsequent studies showed that the rapid decay of the correlator $g^{(1)}$ with distance is related to the simultaneous excitation of several spatial modes [66]. Only when pumping with a laser beam with a Gaussian transverse profile, which excites a single, lowest-energy mode, does the exponent coincide with the theoretical one near the threshold of the BKT condensate emergence and becomes even smaller with increasing photoexcitation intensity [67].

It should be clarified that the results shown in Fig. 16b were obtained by tuning to the main maximum of the PRR signal: at $\lambda = \lambda_{\rm max}$. Here, the pump spot size was ≈ 5 μm, the probe spot size was ≈ 50 μm, and the size of the spreading region was ≈ 20 μm, i.e., PRR was detected for SCEs not in the energy minimum, at $q \simeq 1/l_{\rm B}$, but at $q \approx 0$. Subsequently, interferometric measurements were performed on all less

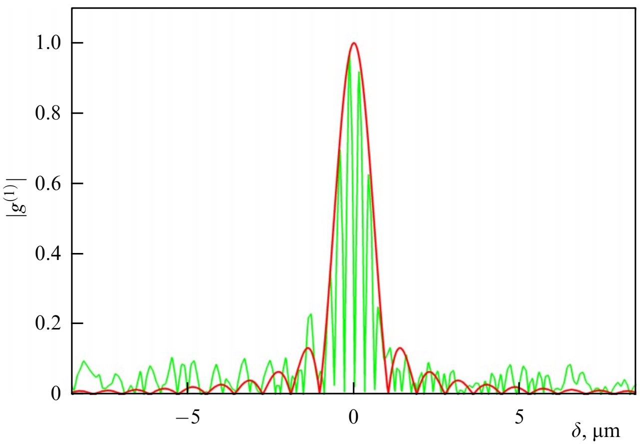

Figure 17. Coherence of the magnetoexcitation ensemble in a fractional quantum Hall insulator at $\nu = 1/3$, $P_{\text{pump}} = 80$ μW. The green line is the profile of interference fringes in PRR light: $|g^{(1)}(\delta) \cos \Phi(\delta)|$. The red curve is the instrumental function that best describes the central peak. $T \approx 0.55$ K.

intense PRR resonances mentioned in the previous section using a probe spot size of ≈ 100 μm. In no case was a more pronounced macroscopic coherence in the light of PRR observed than that shown in Fig. 16b. No systematic dependence of the interference pattern and the parameter ξ on the resonance wavelength was found. In the regime of SCE spreading over hundreds of micrometers ($\lambda = \lambda_2$), experiments were performed with the registration of interference at a distance of up to ~ 100 μm from the pump spot. The assumption that the component with a coherence length of $\xi \gtrsim 10$ μm is associated precisely with the far-spreading SCEs was not confirmed.

Figure 17 shows the results of interferometric measurements characteristic of a magnetograviton condensate at a filling factor $\nu = 1/3$. The data were obtained using the same experimental setup and measurement technique as in the previous case, at $\nu = 2$. Note that the character of the distribution $|g^{(1)}(\delta)|$ remains unchanged over a wide range of pump powers. Obviously, the spatial coherence length of the light resonantly reflected from the photoexcited Laughlin liquid is well below the spatial resolution of ≈ 1 μm provided by the recording optical system.

4. Conclusion

The magnetoexciton condensate is the first experimental example of the condensation of composite bosons not in ordinary space, as in the case of an electron–hole liquid in bulk semiconductors [68], and not in ordinary momentum space, as in the case of atomic Bose condensates [69], but in the space of generalized momenta — quantities that depend on both spatial coordinates and their gradients [70]. The magnetoexciton (magnetofermionic) condensate is formed from dark cyclotron spin magnetoexcitons with a dipole moment of the order of the magnetic length multiplied by the elementary electronic charge. Due to the impossibility of satisfying the laws of conservation of energy and momentum simultaneously, complete thermalization does not occur in the ensemble of nonequilibrium SCEs. Owing to ultra-long thermalization times, the SCE ensemble is substantially nonequilibrium. It consists of a gas of excitons with generalized momenta $q \approx 0$ (their fraction is determined by temperature, photoexcitation dynamics, intravalley relaxation, and the transport of magnetoexcitons from the excitation spot) and a condensate of magnetoexcitons with momenta $q \approx 1/l_{\text{B}}$, which participate in fast exciton transport, accompanied by spin transfer, over macroscopic distances. Thus, the photoexcited SCE system differs significantly from the system of momentum-space indirect excitons in bulk semiconductors, such as Ge and Si, where long-lived excitons thermalize on the scale of their lifetimes [71]. Parametrically pumped Bose-Einstein condensates of magnons in yttrium iron garnet films should be considered as an example of a nonequilibrium Bose system close to the system of cyclotron spin magnetoexcitons [72].

It can also be concluded generally that the spatial coherence of the investigated magnetoexcitation condensates in quantum Hall insulators correlates with their ability to propagate in real space. The SCE condensate in an integer Hall insulator $\nu = 2$ with $q \approx 0$ possesses high spatial coherence as well as the ability to spread over macroscopic distances. In contrast, the dense ensemble of spin magnetogravitons in the Laughlin liquid $\nu = 1/3$ demonstrates neither spatial coherence nor noticeable spreading. Certainly, it would be interesting to trace the relationship between the coherence and transport properties of excitation ensembles in quantum Hall systems at filling factors other than 2 and 1/3. However, at present, there are no filling factors in integer or fractional quantum Hall systems, except for $\nu = 2$ and $\nu = 1/3$, at which dense long-lived nonequilibrium excitation ensembles could be created. The first optical studies of the excited fractional state $\nu = 2/5$ were recently reported in [73]. There is a possibility that the filling factor 2/5 will become accessible in the foreseeable future for experimental studies similar to those carried out in the present work.

This work was supported by the Russian Science Foundation Grant no. 24-12-00411.

References

1. Moskalenko S A *Sov. Phys. Solid State* **4** 199 (1962); *Fiz. Tverd. Tela* **4** 276 (1962)
2. Blatt J M, Böer K W, Brandt W *Phys. Rev.* **126** 1691 (1962)
3. Casella R C *J. Phys. Chem. Solids* **24** 19 (1963)
4. Keldysh L V, Kozlov A N *JETP Lett.* **5** 190 (1967); *Pis'ma Zh. Eksp. Teor. Fiz.* **5** 238 (1967)
5. Keldysh L V, Kozlov A N *Sov. Phys. JETP* **27** 521 (1968); *Zh. Eksp. Teor. Fiz.* **54** 978 (1968)
6. Cornell E A, Wieman C E *Rev. Mod. Phys.* **74** 875 (2002)
7. Ketterle W *Rev. Mod. Phys.* **74** 1131 (2002)
8. Snoke D, Kavoulakis G M *Rep. Prog. Phys.* **77** 116501 (2014)
9. Sibeldin N N *Phys. Usp.* **60** 1147 (2017); *Usp. Fiz. Nauk* **187** 1236 (2017)
10. Kulakovskii V D, Timofeev V B, in *Electron-Hole Droplets in Semiconductors* (Modern Problems in Condensed Matter Sciences, Vol. 6, Eds C D Jeffries, L V Keldysh) (Amsterdam: North-Holland, 1983) p. 95
11. Lozovik Yu E, Yudson V I *JETP Lett.* **22** 274 (1975); *Pis'ma Zh. Eksp. Teor. Fiz.* **22** 556 (1975)
12. Shevchenko S I *Sov. J. Low Temp. Phys.* **2** 251 (1976); *Fiz. Nizk. Temp.* **2** 505 (1976)
13. Deng H, Haug H, Yamamoto Y *Rev. Mod. Phys.* **82** 1489 (2010)
14. Kukushkin I V, Timofeev V B *Adv. Phys.* **45** 147 (1996)
15. Arora A *J. Appl. Phys.* **129** 120902 (2021)
16. Lerner I V, Lozovik Yu E *Sov. Phys. JETP* **51** 588 (1980); *Zh. Eksp. Teor. Fiz.* **78** 1167 (1980)
17. Lerner I V, Lozovik Yu E *Sov. Phys. JETP* **53** 763 (1981); *Zh. Eksp. Teor. Fiz.* **80** 1488 (1981)
18. Butov L V et al. *Phys. Rev. B* **60** 8753 (1999)
19. Dickmann S *Phys. Rev. Lett.* **110** 166801 (2013)

20. Kohn W *Phys. Rev.* **123** 1242 (1961)
21. Bychkov Yu A, Iordanskii S V, Eliashberg G M *JETP Lett.* **33** 143 (1981); *Pis'ma Zh. Eksp. Teor. Fiz.* **33** 152 (1981)
22. Kallin C, Halperin B I *Phys. Rev. B* **30** 5655 (1984)
23. Kulik L V et al. *Phys. Rev. B* **72** 073304 (2005)
24. Dickmann S, Kukushkin I V *Phys. Rev. B* **71** 241310 (2005)
25. Kulik L V et al. *Sci. Rep.* **5** 10354 (2015)
26. Kulik L V et al. *Phys. Usp.* **62** 865 (2019); *Usp. Fiz. Nauk* **189** 925 (2019)
27. Kulik L V et al. *Nature Commun.* **7** 13499 (2016)
28. Hohenberg P C *Phys. Rev.* **158** 383 (1967)
29. Mermin N D, Wagner H *Phys. Rev. Lett.* **17** 1133 (1966)
30. Berezinskii V L *Sov. Phys. JETP* **32** 493 (1971); *Zh. Eksp. Teor. Fiz.* **59** 907 (1970); Berezinskii V L *Sov. Phys. JETP* **34** 610 (1972); *Zh. Eksp. Teor. Fiz.* **61** 1144 (1971)
31. Kosterlitz J M, Thouless D J *J. Phys. C* **6** 1181 (1973)
32. Bishop D J, Reppy J D *Phys. Rev. Lett.* **40** 1727 (1978); *Phys. Rev. B* **22** 5171 (1980)
33. van der Zant H S J, Rijken H A, Mooij J E *J. Low Temp. Phys.* **82** 67 (1991)
34. Hadzibabic Z et al. *Nature* **441** 1118 (2006)
35. Cladé P et al. *Phys. Rev. Lett.* **102** 170401 (2009)
36. Roumpos G et al. *Nature Phys.* **7** 129 (2011)
37. Eisenstein J P, MacDonald A H *Nature* **432** 691 (2004)
38. Kulik L V et al. *Nature Commun.* **12** 6477 (2021)
39. Kulik L V et al. *Appl. Phys. Lett.* **123** 083101 (2023)
40. Kulik L V et al. *JETP Lett.* **118** 455 (2023); *Pis'ma Zh. Eksp. Teor. Fiz.* **118** 462 (2023)
41. Larionov A V et al. *JETP Lett.* **120** 434 (2024); *Pis'ma Zh. Eksp. Teor. Fiz.* **120** 451 (2024)
42. Bartolomei H et al. *Science* **368** 173 (2020)
43. Nakamura J et al. *Nature Phys.* **16** 931 (2020)
44. Zhuravlev A S et al. *Phys. Rev. B* **89** 161301 (2014)
45. Eriksson M A et al. *Phys. Rev. Lett.* **82** 2163 (1999)
46. Groshaus J G et al. *Phys. Rev. Lett.* **98** 156803 (2007)
47. Zhuravlev A S et al. *Phys. Rev. Lett.* **117** 196802 (2016)
48. Kuznetsov V A et al. *Phys. Rev. B* **98** 205303 (2018)
49. Born M, Wolf E *Osnovy Optiki* (Moscow: Nauka, 1973); Translated from English: *Principles of Optics* (Oxford: Pergamon Press, 1968)
50. Roumpos G et al. *Proc. Natl. Acad. Sci. USA* **109** 6467 (2012)
51. Kulik L V et al. *Phys. Rev. B* **79** 121310 (2009)
52. Koreyev A S et al. *Phys. Rev. B* **110** 165417 (2024)
53. Ando T, Fowler A B, Stern F *Rev. Mod. Phys.* **54** 437 (1982)
54. Dickmann S, Kulik L V, Kuznetsov V A *Phys. Rev. B* **100** 155304 (2019)
55. Kulik L V et al. *Sci. Rep.* **8** 10948 (2018)
56. Gorbunov A V et al. *JETP Lett.* **106** 682 (2017); *Pis'ma Zh. Eksp. Teor. Fiz.* **106** 651 (2017)
57. Kulik L V et al. *Appl. Phys. Lett.* **114** 062403 (2019)
58. Gorbunov A V et al. *Ann. Physik* **531** 1800443 (2019)
59. Zhuravlev A S et al. *JETP Lett.* **110** 284 (2019); *Pis'ma Zh. Eksp. Teor. Fiz.* **110** 260 (2019)
60. Dickmann S, Kaysin B D *JETP Lett.* **114** 585 (2021)
61. Gorbunov A V et al. *JETP Lett.* **116** 779 (2022); *Pis'ma Zh. Eksp. Teor. Fiz.* **116** 756 (2022)
62. Gorbunov A V et al. *J. Appl. Phys.* **132** 244301 (2022)
63. Gorbunov A V et al. *Bull. Ross. Acad. Nauk Phys.* **87** 141 (2023); *Izv. Ross. Akad. Nauk Ser. Fiz.* **87** 167 (2023)
64. Gorbunov A V et al. *JETP Lett.* **114** 417 (2021); *Pis'ma Zh. Eksp. Teor. Fiz.* **114** 479 (2021)
65. Gorbunov A V, Timofeev V B *Bull. Ross. Acad. Nauk Phys.* **86** 380 (2022); *Izv. Ross. Akad. Nauk Ser. Fiz.* **86** 467 (2022)
66. Nitsche W H et al. *Phys. Rev. A* **93** 053622 (2016)
67. Nitsche W H et al. *Phys. Rev. B* **90** 205430 (2014)
68. Keldysh L V *Contemp. Phys.* **27** 395 (1986)
69. Anglin J R, Ketterle W *Nature* **416** 211 (2002)
70. Avron J E, Herbst I W, Simon B *Ann. Phys.* **114** 431 (1978)
71. Kukushkin I V, Kulakovskii V D, Timofeev V B *JETP Lett.* **34** 34 (1981); *Pis'ma Zh. Eksp. Teor. Fiz.* **34** 36 (1981)
72. Demokritov S O et al. *Nature* **443** 430 (2006)
73. Knüppel P et al. *Nature* **572** 91 (2019)